Dependence of surface plasmon-phonon-polariton in 4 H-SiC on free carrier concentration

H. Karakachian and M. Kazan

Citation: Journal of Applied Physics **121**, 093103 (2017); doi: 10.1063/1.4977873
View online: http://dx.doi.org/10.1063/1.4977873
View Table of Contents: http://aip.scitation.org/toc/jap/121/9
Published by the American Institute of Physics

Dependence of surface plasmon-phonon-polariton in 4 H-SiC on free carrier concentration

H. Karakachian and M. Kazan[a)]
Department of Physics, American University of Beirut, P.O. Box 11-0236, Riad El-Solh, Beirut 1107-2020, Lebanon

(Received 7 October 2016; accepted 20 February 2017; published online 6 March 2017)

In this paper, we present a thorough study of the characteristics of the surface modes that result from coupling between plasmon electronic oscillation modes, phonon modes, and electromagnetic modes. The Fourier transform of *p*-polarized reflectivity measurements were carried out on different 4 H-SiC epilayers differing in their free carrier concentration. The reflectivity measurements were performed with appropriate care to record reflectivity spectra averaged over a wide range of incidence angles. The complex infrared dielectric functions of the measured samples were determined by correcting the values obtained from the conventional Kramers-Kronig conversion technique with reference to Fresnel equations for reflectivity. The obtained dielectric functions were used to compute the effect of the free carrier concentration and the resulting plasmon electronic oscillation on the dispersion spectrum, lifetime, mean propagation length of the bulk, and surface plasmon-phonon-polariton modes. The effect of the free carrier concentration on the temporal coherence of surface plasmon-phonon-polariton is investigated, showing a potential practical method for enhancing the temporal coherence of SiC based thermal sources. *Published by AIP Publishing*. [http://dx.doi.org/10.1063/1.4977873]

I. INTRODUCTION

In the last few decades, nanophotonics emerged as a frontier research to exploit the interaction of nanoscale phenomena with electromagnetic waves and the nanoscale confinement and guidance of these waves.[1–5] Extensive research has been conducted to exploit in particular, the confinement and guidance of electromagnetic energy at the surface of a material.[6–8] The confinement and guidance of electromagnetic energy on the surface of metals in the form of surface plasmon waves have attracted wide interest, but unfortunately, losses due to plasmon waves scattering are significant, making light confinement and guidance at the surface somehow problematic.[9–11]

In a polar material, the frequencies of the zone center optical phonon modes are split into longitudinal optical and transverse optical components by the internal macroscopic electric field. This macroscopic electric field serves to stiffen the force constant of the phonon and thereby raise the frequency of the longitudinal optical phonon (ω_{LO}) over that of the transverse optical phonon (ω_{TO}). The frequency range bounded by ω_{TO} and ω_{LO} is known as the Reststrahlen band. Within the Reststrahlen band, the real part of the material response to an electromagnetic excitation $\mathrm{Re}(\varepsilon)$ is negative. This has the consequence that within the Reststrahlen band, electromagnetic plane waves acquire an evanescent character giving rise to modes confined at the surface. These surface modes are known as the surface phonon-polariton (SPhP) modes. Hence, the SPhP can be regarded as surface electromagnetic waves arising from the coupling of electromagnetic modes (photons) with lattice vibration modes (optical phonons) in polar dielectric materials.[9,12,13] Relevant research works suggested that the lifetime of SPhP is orders of magnitude larger than that of surface plasmon.[14,15] This makes SPhP a potential candidate for enhancing the lifetime of electromagnetic energy confined at the surface, contributing to many technological applications in the field of nanophotonics. As such, it has been demonstrated that the SPhP modes are the dominant energy carriers in the near-field and their diffraction by gratings introduced on the material surface produces coherent infrared emission in the far-field.[16–21]

In an *n*-doped polar material, the presence of free carriers in the volume of the material results in plasmon electronic longitudinal oscillation modes. Due to their longitudinal nature, these plasmon electronic oscillation modes can couple to only longitudinal optical phonon modes to give rise to a mixed character longitudinal modes of frequencies higher than those of the original longitudinal optical phonon modes.[22,23] These modes are known as the LOPC modes. On the surface, however, the plasmon electronic oscillation modes acquire transverse components and hence can couple to transverse surface optical modes.

Indeed, it is highly desirable to examine the interaction and coupling of incident electromagnetic modes with phonon-plasmon mixed character modes both on the surface and in the volume because understanding the underlying mechanisms governing the characteristics of the resultant waves, which will be referred to as the plasmon-phonon-polariton (PPhP) modes, can help to rationally design systems for numerous technological applications in nanophotonics.

Phonon-plasmon interactions have been observed by infrared (IR) spectroscopic ellipsometry upon understanding the physical origins of the Berremann-effect.[22,23] The mechanisms involved in coupling these two different modes have

a)Author to whom correspondence should be addressed. Electronic mail: mk140@aub.edu.lb

also been explained in the literature.[24,25] In this paper, we tackle the particular issue of the coupling between incident electromagnetic modes with phonon-plasmon mixed character modes and present a detailed description on how the free carrier concentration in the crystal affects the characteristics (lifetime, mean-propagation-length, and, most importantly, temporal coherence) of the resultant plasmon-phonon-polariton (PPhP) modes both in the volume and on the surface of the crystal. One of the key developments presented in this paper is that the response functions of the samples investigated are obtained without the use of any physical models or assumptions. They are obtained by correcting the values found from the Kramers-Kronig conversion technique with reference to Fresnel equations for reflectivity.[26]

The material being used to investigate the characteristics of the volume and surface PPhP modes is 4 H-SiC. The choice of 4 H-SiC is beneficial due to the availability of large area highly crystalline 4 H-SiC epilayers, the availability of techniques for doping and controlling the free carrier concentration in SiC, and due to the fact that the Reststrahlen band of 4 H-SiC lies in the spectral range where the response of the commonly used infrared detectors is linear.[9] However, we believe that the fundamental physics outlined in this paper is applicable in all *n*-type polar semiconductors.

II. EXPERIMENTS

The experiments were carried out on three *c*-oriented 4 H-SiC epilayers (8° off-axis) deposited on unintentionally *n*-doped 500 μm thick 4 H-SiC substrates. The epilayers were 3 μm thick and of $2 \times 10^{15}\,\mathrm{cm}^{-3}$ initial free carrier concentration. Two of the investigated samples were implanted with different doses of N-ions.[27] The energy of the implantation of the N-ions was decreased from 5.5 MeV to zero systematically in 60 steps in order to ensure uniform distribution of N-ions over the thickness of the implanted epilayer. The implanted samples were then encapsulated with a C cap. The C capping layer was formed by thermal conversion during annealing at 750 °C for 30 min of a spin-coated AZ5214E photoresist layer deposited on the SiC implanted epilayers in a conventional quartz tube furnace under N flux.

For the sake of defect recovery after ion implantation and n dopants activation, the implanted samples were annealed at 1650 °C in an RF-induction furnace under an Ar atmosphere during 45 min with a heating ramp-up at 40 °C/s. Lastly, the capping layer was removed by the O_2 plasma in an Alcatel Nextral NE110 RIE reactor. These annealing conditions have been optimized to preserve the root-mean-square surface roughness and lead to a good activation of the N dopants. Hall effect (in standard Van der Pauw geometry) measurements were employed to measure the carrier concentration and mobility in the implanted epilayers. The free carrier concentration and mobility were measured to be $10^{17}\,\mathrm{cm}^{-3}$ and $620\,\mathrm{cm}^2\,\mathrm{V}^{-1}\,\mathrm{s}^{-1}$ in the slightly implanted epilayer and $10^{19}\,\mathrm{cm}^{-3}$ and $105\,\mathrm{cm}^2\,\mathrm{V}^{-1}\,\mathrm{s}^{-1}$ in the heavily implanted epilayer. The low carrier mobility in the heavily implanted sample suggests that the adopted annealing process does not remedy all the defects generated by the ion implantation. However, as will be shown below, the ion implantation does not alter the frequency of the transverse phonons. This clearly demonstrates that the ion implantation did not cause extended defects or polymorphism change, and the defects formed are most likely point-like defects that do not alter macroscopic properties such as the dielectric function. Hence, the carrier concentration, which determines the plasmon electronic oscillation frequency, is taken as the only parameter in our work.

Far-field infrared reflectivity measurements were performed on the samples described above. The irradiation of the sample with infrared light and the collection of the reflected infrared light are schematically depicted in Fig. 1. The incident beam was *p*-polarized and at 45° from the normal to the sample surface. The incident beam was first expanded and then focused on the surface of the sample, and the reflected light was collected using an integrating sphere in order to record reflectivity spectra averaged over a wide range of incidence angles. The collected light was then collimated, and the reflectivity spectrum was obtained using the standard Michelson interferometry technique. A DTGS detector and a KBr beamsplitter were used, and spectra were recorded in the 400–3500 cm^{-1} frequency range. The reflectivity of each sample was compared to that of a gold coated mirror, and the reproducibility of the measurements was checked by measuring each spectrum twice. The two recorded data from each sample were identical within the experimental error, i.e., within 1% reflectivity.

III. ANALYSIS OF THE REFLECTIVITY AND DIELECTRIC SPECTRA BY A CORRECTED KRAMERS-KRONIG CONVERSION TECHNIQUE

Reflectivity measurements were carried out in order to deduce from measurements the effective complex dielectric functions of the samples investigated for *p*-polarized incident light. The usual way of deducing the complex dielectric function from a reflectivity spectrum is to determine the frequency-dependent amplitude $\rho(\omega)$ and phase $\theta(\omega)$ separately using the Kramers-Kronig conversion technique and then the complex dielectric function, or alternatively, the

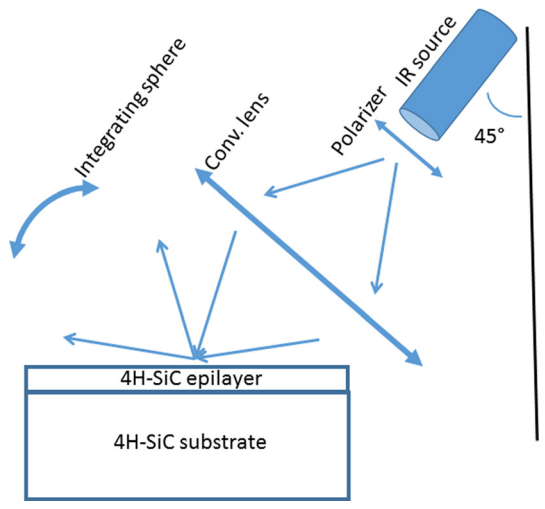

FIG. 1. Experimental configuration for recording reflectivity spectra averaged over a wide range of incidence angles.

real and imaginary parts of the complex refractive index $N(\omega) = n(\omega) + ik(\omega)$. This conversion technique requires an integration of the reflectivity spectrum from zero to infinity. The experimental data, however, are always obtained within a finite range of frequency (in our case between $400\,\mathrm{cm}^{-1}$ and $3500\,\mathrm{cm}^{-1}$). The common way out of this problem is to artificially extrapolate the values at hand to zero and infinity despite the fact that this leads to high margin of error in the results especially at the boundaries of the measured frequency range.[21,28] Therefore, we proceed by correcting the solutions for $n(\omega)$ and $k(\omega)$ obtained from Kramers-Kronig integral.

A. Method for correcting the Kramers-Kronig conversion

To determine the dielectric properties of the epilayers investigated, we need to determine the dielectric properties of the substrate on which they are deposited. To determine the dielectric properties of the substrate, we first measure the reflectivity spectrum of the substrate (the reflectivity spectrum from the back side of the sample) and deduce its complex refractive index by using the Kramers-Kronig integral.

According to the Kramers-Kronig theorem, the phase equation can be written as

$$\theta(\omega) = -\frac{1}{2}\int_0^{\infty} \ln\left|\frac{\Omega+\omega}{\Omega-\omega}\right| \frac{d}{d\Omega}[\ln R(\Omega)]d\Omega, \tag{1}$$

where ω is the measured frequency and Ω is the integration variable. In order to implement Eq. (1), we write it in the form

$$\theta(\omega) = -\frac{1}{2}\left[\begin{array}{l} \int_0^{\Omega_0} \ln\left|\frac{\Omega+\omega}{\Omega-\omega}\right| \frac{d}{d\Omega}[\ln R(\Omega)]d\Omega \\ +\int_{\Omega_0}^{\Omega_f} \ln\left|\frac{\Omega+\omega}{\Omega-\omega}\right| \frac{d}{d\Omega}[\ln R(\Omega)]d\Omega \\ +\int_{\Omega_f}^{\infty} \ln\left|\frac{\Omega+\omega}{\Omega-\omega}\right| \frac{d}{d\Omega}[\ln R(\Omega)]d\Omega \end{array}\right], \tag{2}$$

where Ω_0 and Ω_f determine the low and high frequency ends of the measured spectrum. We determine $R(\Omega)$ in the first integral of Eq. (2) by extrapolating the measured reflectivity spectrum to zero using the Lorentz-Drude model. Then, the first integral in the phase equation can be readily solved. To solve the second integral, we write it in the form

$$\int_{\Omega_0}^{\Omega_1} d\Omega + \int_{\Omega_1}^{\Omega_2} d\Omega + \ldots \int_{\Omega_{i-1}}^{\Omega_i} d\Omega + \ldots \int_{\Omega_{f-1}}^{\Omega_f} d\Omega, \tag{3}$$

and in each interval $[\Omega_{i-1}, \Omega_i]$(which determines the experimental spectral resolution), we approximate the reflectivity with a linear fit. Then, we obtain the value of the second integral by solving each elementary integral numerically and summing over all the individual integrals. We determine the analytical expression of $R(\omega)$ in the third integral by extrapolating the reflectivity spectrum to infinity using pure mathematical functions and then we solve the third integral numerically. We believe that the arbitrary extrapolation of the reflectivity in the third integral can be a source of error in the determination of the phase. The error on the overall phase depends on the variation of the reflectivity spectrum beyond the measured frequency range. If the reflectivity spectrum saturates beyond the measured frequency range, the contribution of the third integral to the overall phase is nil, and the phase obtained by the Kramers-Kronig conversion technique is highly accurate. However, if the reflectivity spectrum beyond the measured frequency range varies, the contribution of the third integral to the overall phase in the measured frequency range is an angle that slowly increases as we move towards the high frequency end of the measured spectrum. We present below the procedure we follow for correcting the dielectric properties obtained from the Kramers-Kronig integral.

Let us denote the substrate complex refractive index obtained from Kramers-Kronig by $N_s'(\omega) = n_s'(\omega) + ik_s'(\omega)$. Since the thickness of the substrate is much greater than its skin depth, we can consider the substrate as a semi-infinite medium. In that limit, the Fresnel coefficient of reflectivity can be written as[29]

$$r_{//s} = \frac{E_{//r}}{E_{//i}} = \frac{-N_s\cos\theta_i + \cos\theta_t}{N_s\cos\theta_i + \cos\theta_t}, \tag{4}$$

for an incident and reflected electric field in the plane of incidence, and

$$r_{\perp s} = \frac{E_{\perp r}}{E_{\perp i}} = \frac{\cos\theta_i - N_s\cos\theta_t}{\cos\theta_i + N_s\cos\theta_t} \tag{5}$$

for an incident and reflected electric field perpendicular to the plane of incidence. Here, $E_{//i}$ and $E_{//r}$ are the incident and reflected electric fields in the plane of incidence, $E_{\perp i}$ and $E_{\perp r}$ are the incident and reflected electric fields perpendicular to the plane of incidence, θ_i and θ_t are the angle of incidence and the angle of refraction, and $N_s = N_s(\omega) = n_s(\omega) + ik_s(\omega)$ is the exact complex refractive index of the substrate. The angles θ_i and θ_t are related according to Snell's law $\theta_t = \sin^{-1}\left(\frac{\sin\theta_i}{N_s}\right)$. In the case where both the incident electric field E_i and reflected electric filed E_r are unpolarized, the Fresnel coefficient of reflectivity takes the general form

$$r_s = \frac{E_r}{E_i}. \tag{6}$$

Now, if we consider that φ is the angle between the incident electric field and the plane of incidence and χ is the angle between the reflected electric field and the plane of incidence, then Eq. (6) can be written as

$$r_s = \frac{E_r}{E_i} = \frac{E_{//r}}{E_{//i}} \times \frac{\cos\varphi}{\cos\chi} = \frac{E_{\perp r}}{E_{\perp i}} \times \frac{\sin\varphi}{\sin\chi}. \tag{7}$$

Upon substituting Eqs. (4) and (5) in Eq. (7), we can write

$$\chi = \tan^{-1}\left(\tan\varphi \frac{r_{\perp s}}{r_{//s}}\right). \tag{8}$$

Thus, according to Eq. (8), if the incident light is *p*-polarized (i.e., the incident electric field is polarized in the plane of incidence), the reflected light is also *p*-polarized, and the measured reflectivity should satisfy the condition $R - r_{//s}r^*_{//s} = 0$. Since the measurements in the present work were carried out with *p*-polarized incident light and the recorded spectra represent average reflectivity spectra over all angles of incidence, the measured reflectivity of the substrate should satisfy the equation

$$R(\omega) - \frac{2}{\pi}\int_0^{\frac{\pi}{2}} r_{//s}(\theta_i,\omega)r^*_{//s}(\theta_i,\omega)d\theta_i = 0. \tag{9}$$

In order to determine the exact complex refractive index of the substrate $N_s(\omega) = n_s(\omega) + ik_s(\omega)$, we give a range of possible values for $n_s(\omega)$ and $k_s(\omega)$ in the vicinity of $n'_s(\omega)$ and $k'_s(\omega)$(which are previously obtained from the Kramers-Kronig integral). For instance, we take a range of values for $n_s(\omega)$ where the maximum is 50% greater than $n'_s(\omega)$ and the minimum is 50% smaller than $n'_s(\omega)$ with small steps of 0.001. We also define a range for $k_s(\omega)$ using the same approach. Then, we take $n_s(\omega)$ as a row vector and $k_s(\omega)$ as a column vector to form a mesh with cells corresponding to all possible combinations of $n_s(\omega)$ and $k_s(\omega)$ in the vicinity of the values obtained from the Kramers-Kronig integral. We solve Eq. (9) for each cell of the mesh. The combination of $n_s(\omega)$ and $k_s(\omega)$ that gives the best solution to Eq. (9) will serve as the actual value of the substrate complex refractive index $N_s(\omega)$. We repeat this procedure at each measured frequency to obtain $n_s(\omega)$ and $k_s(\omega)$ spectra.

Once the exact refractive index of the substrate $N_s(\omega)$ is obtained, we deduce the exact complex refractive index of the epilayer $N(\omega) = n(\omega) + ik(\omega)$ by using the following method. We measure the reflectivity spectrum from the surface of the epilayer. In our case, this reflectivity spectrum is largely determined by the epilayer. This is because the refractive index of the 4 H-SiC substrate is very close to that of the lowest doped 4 H-SiC epilayer (which drastically decreases the probability of light reflection at the interface between the epilayer and the substrate) and the plasmon electron oscillation in the doped epilayers damps the light rapidly and reduces significantly the skin depth in the epilayers (which make the contribution of the substrate to the overall reflectivity spectrum unlikely). Hence, the Kramers-Kronig conversion of the reflectivity spectrum from the epilayer surface provides an approximated complex refractive index of the epilayer. We denote this approximated epilayer complex refractive index by $N'(\omega) = n'(\omega) + ik'(\omega)$. On the other hand, upon using the transfer matrix method, it can be shown that the Fresnel coefficient of reflectivity from the epilayer-substrate system for a *p*-polarized incident light can be written as[29]

$$r_{//} = \frac{\left(m_{11} + \frac{1}{p_3}m_{12}\right) - \left(m_{21} + \frac{1}{p_3}m_{22}\right)p_1}{\left(m_{11} + \frac{1}{p_3}m_{12}\right) + \left(m_{21} + \frac{1}{p_3}m_{22}\right)p_1}, \tag{10}$$

where $p_i = \frac{\cos\theta_i}{\left(\frac{N_i}{\mu c}\right)}$ is the impedance of the *i*th surface in the air/epilayer/substrate system with N_i being the complex index of refraction of the *i*th medium, μ the magnetic permeability, c the speed of light in vacuum, and θ_i the angle of incidence in the *i*th medium. The angles of incidence in the three media (air/epilayer/substrate) are related to each other according to Snell's law. The m_{ij} in Eq. (10) are the elements of the interference matrix

$$M = \begin{pmatrix} \cos\phi_2 & -ip_2\sin\phi_2 \\ -ip_2\sin\phi_2 & \cos\phi_2 \end{pmatrix}, \tag{11}$$

where $\phi_2 = \frac{\omega N d\cos\theta_2}{c}$, with ω being the angular frequency, N the complex index of refraction of the epilayer, and d the epilayer thickness. The measured reflectivity from the epilayer-substrate system should satisfy the equation

$$R(\omega) - \frac{2}{\pi}\int_0^{\frac{\pi}{2}} r_{//}(\theta_i,\omega)r^*_{//}(\theta_i,\omega)d\theta_i = 0. \tag{12}$$

Since the complex index of refraction of the substrate N_s(or N_3) is known, the only unknown parameter in Eq. (12) is the exact complex index of refraction of the epilayer $N(\omega) = n(\omega) + ik(\omega)$. In order to determine $N(\omega)$, we give a range of possible values for $n(\omega)$ and $k(\omega)$ in the vicinity of $n'(\omega)$ and $k'(\omega)$ (which are obtained by converting the reflectivity from the epilayer surface using the Kramers-Kronig integral). Then, we take $n(\omega)$ as a row vector and $k(\omega)$ as a column vector to form a mesh with cells corresponding to all possible combinations of $n(\omega)$ and $k(\omega)$ in the vicinity of the values obtained from the Kramers-Kronig integral. We solve Eq. (12) for each cell of the mesh. The combination of $n(\omega)$ and $k(\omega)$ that gives the best solution to Eq. (12) will serve as the actual value of the epilayer complex refractive index $N(\omega)$. We repeat this procedure at each measured frequency to obtain $n(\omega)$ and $k(\omega)$ spectra. From the knowledge of $n(\omega)$ and $k(\omega)$, the real and imaginary parts of the complex dielectric function of the epilayer can be readily obtained.

B. Complex refractive indices of the samples investigated obtained from the corrected Kramers-Kronig technique

The measured reflectivity spectra and the complex refractive indices of the samples investigated, as obtained from the corrected Kramers-Kronig technique described above, are shown in Fig. 2. The real and imaginary parts of the complex refractive index of the lowest doped sample obtained from a standard Kramers-Kronig conversion (KK) are also plotted in Fig. 2 for the sake of comparison. As can be noticed, a significant effect of free carrier concentration on both the real and imaginary parts of the complex refractive index is observed at the resonance. Furthermore, the discrepancy between the curves obtained from the corrected Kramers-Kronig technique and those obtained from the standard Kramers-Kronig technique is intensified as the carrier concentration is increased in the sample.

In order to verify the reliability of the corrected Kramers-Kronig technique used in this work to obtain the dielectric properties of the samples investigated, we back calculated the reflectivity spectra using the obtained complex

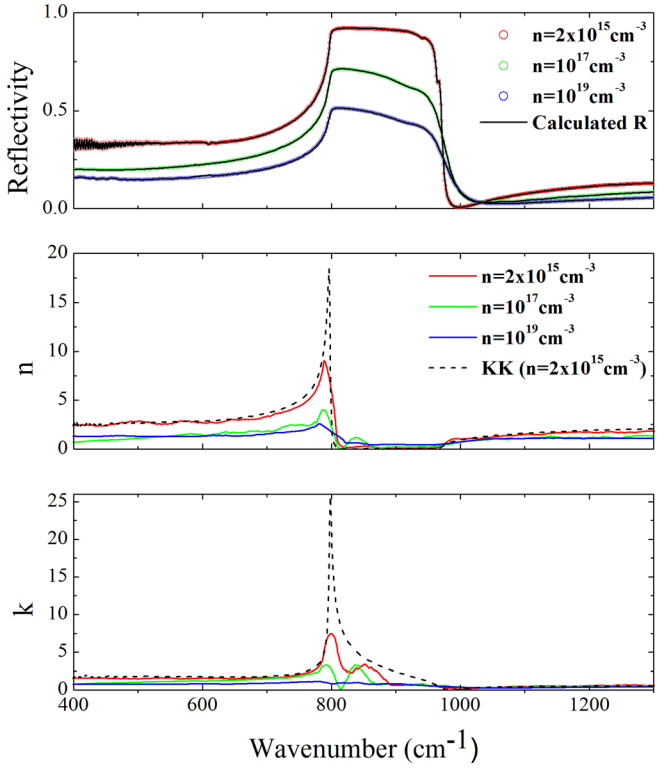

FIG. 2. Reflectivity spectra and real and imaginary parts of the complex refractive indices of the samples investigated. Solid lines: Real and imaginary parts of the refractive indices obtained by using the Kramers-Kronig technique corrected with reference to Fresnel equations for reflectivity. Dashed lines: Real and imaginary parts of the refractive index of the lowest doped sample obtained by using the conventional Kramers-Kronig conversion technique. The reflectivity spectra are back calculated using the real and imaginary parts of the refractive indices obtained from the corrected Kramers-Kronig technique. The measured reflectivity spectra are plotted with symbols. The back calculated reflectivity spectra are plotted with solid lines.

refractive indices of the epilayers and substrates. The back calculated reflectivity spectra of the samples investigated are plotted together with the measured ones. The excellent agreement between the curves demonstrates the reliability of the conversion technique being used.

Finally, it is worth noting that the widely used Lorentz-Drude model offers a simplified description of the complex dielectric function. In that model, random values are usually taken for the phonon and free carrier damping rates and they assumed to be constant over the entire frequency spectrum.[30] This rather crude simplification is proven to be inaccurate in the literature.[31] Thus, the method used in the present work to deduce the dielectric properties of the samples investigated has the advantage of providing a better description to the material response function, which stands as the primary component in understanding the plasmon-phonon-polariton coupling.

IV. RESULTS AND DISCUSSION

As described earlier, surface and volume PPhP modes result from the interaction and coupling of free carriers' collective oscillation modes, zone center optical phonon modes, and incident electromagnetic modes, meaning that their properties depend highly on the characteristics of the zone center optical phonon modes in the material. Therefore, in order to investigate the effect of the free carrier concentration on the PPhP modes, it is highly advantageous to understand first their effect on these optical phonon modes.

A. The effect of plasmon electronic oscillation on the zone center optical phonons

The real (ε_1) and imaginary (ε_2) parts of the dielectric functions and the energy loss functions $\left(\text{Imag}\left(\frac{-1}{(\varepsilon_1+i\varepsilon_2)}\right)\right)$ of the epilayers investigated are shown in Fig. 3. The frequencies and lifetimes of the zone center transverse optical phonon modes and longitudinal LOPC mixed character modes are the principal determinants of these functions. The peak of the imaginary part of the dielectric function is directly related to the absorption of infrared light by transverse optical phonon modes. It occurs at the frequency of the transverse optical phonon, and its width is related to the transverse optical phonon lifetime according to the Heisenberg uncertainty principle.[32,33] It can be seen from Fig. 3 that both the resonance frequency and lifetime of the transverse optical phonon are almost unaffected by the presence of plasmon electronic oscillation modes in the sample. We found that the lifetime of the zone center transverse optical phonon in the lowest doped sample is 1.40 ps, reduced to 1.23 ps and 1.10 ps as the carrier concentration is increased. The independence of the resonance frequency and lifetime of the transverse optical phonon on the free carrier concentration is due to the fact that the transverse optical phonon modes do not couple to plasmon electronic oscillation modes. The

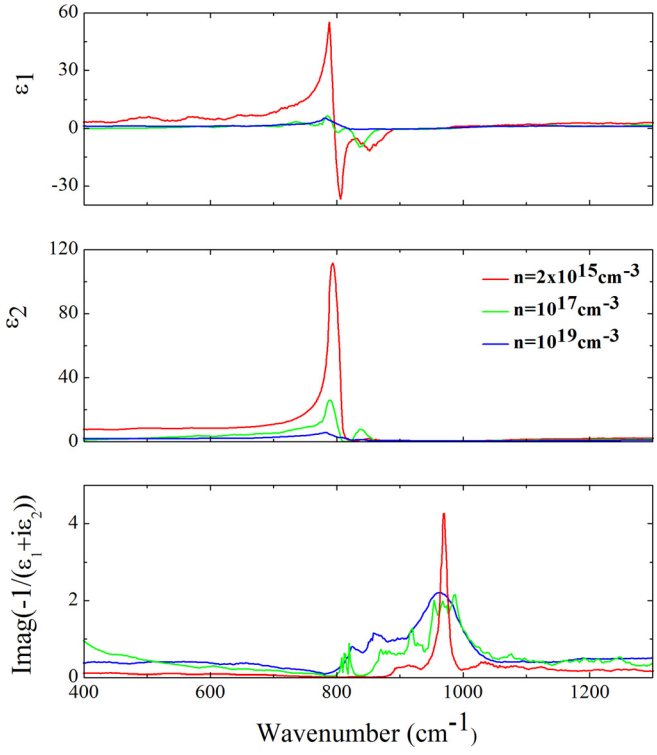

FIG. 3. The dielectric properties of the samples investigated obtained from the corrected the Kramers-Kronig technique.

small lifetime decay is basically due to optical phonon scattering by point-defects induced by the implantation of the N-ions in the 4 H-SiC epilayers.

The peak of the energy loss function of the epilayer is determined by the frequency and lifetime of the LOPC modes in the epilayer.[32,33] Its position occurs at the resonance frequency of the LOPC mode, and its width describes the lifetime of the LOPC mode. Unlike the transverse optical phonon, the lifetime of the LOPC mode is a strong function of the carrier concentration. We observe a lifetime of about 2.25 ps in the lowest doped sample, which strongly decays as the carrier concentration is increased. These results are in good agreement with previously observed Raman spectra broadenings in *n*-type 4 H-SiC free standing crystals.[22,23,34–39] The fact that the coupling of the longitudinal optical phonon to the plasmon electronic oscillation is clearly mirrored in the dielectric functions in Fig. 3 adds a strong support to the reliability of the technique used to deduce the dielectric functions of the samples investigated from reflectivity measurements.

It is worth noting that the LOPC mixed character modes are usually observed in Raman spectra, and their lifetimes are usually estimated from the Raman line shape and position. However, in the case of homoepitaxial multi-layered systems, Raman spectroscopy loses some accuracy as the Raman signal from the substrate superposes to that from the epilayer. In that case, infrared spectroscopy can be more quantitative than Raman spectroscopy because, as described in Subsection IV A, the homoepitaxial multi-layered system linear response to an infrared wavelength excitation can be described by a simple theory and the deconvolution of the substrate response and epilayer response can be carried out precisely to yield quantitative results.

B. Bulk plasmon-phonon-polariton

The observed reduction in the intensity of the reflectivity and dielectric spectra as the free carrier concentration increases is due to the absorptive nature of the plasmon electronic oscillation in the volume of the crystal. Thus, these spectra can be used to see how the plasmon electronic oscillation affects the electromagnetic wave propagating in the volume of an *n*-doped polar crystal. In other words, these spectra can be used to investigate the PPhP wave in the volume of the crystal as a function of the free carrier concentration. The general dispersion relations of such an electromagnetic wave are given by[40]

$$(ck)^2 = \varepsilon(\omega)\omega^2, \tag{13}$$

where ω and k are the angular frequency and wavevector (oriented parallel to the surface) of the PPhP wave propagating in the crystal, c is the speed of light in vacuum, and $\varepsilon(\omega)$ is the complex dielectric function of the crystal under consideration. In order to determine the lifetime of the resultant bulk PPhP, we consider a real wavevector and a complex frequency $\omega = \omega' + i\omega''$ and solve Eq. (13) numerically. The function $\omega'(k)$ determines the dispersion of the bulk PPhP, and the inverse of the function $\omega''(k)$ gives the lifetime of each bulk PPhP mode. Thus, the dispersion curves and mode lifetimes have an implicit dependence on the characteristics of the optical phonon modes and plasmon electronic oscillation modes through $\varepsilon(\omega)$.

The computed PPhP dispersion curves and the mode lifetimes in the 4 H-SiC epilayers investigated are illustrated in Fig. 4. We found that the lowest doped epilayer exhibits a peak lifetime value of 0.3 ps at around 998 cm^{-1}, and the N-implanted samples exhibit a peak lifetime value 70% lower than the lowest doped epilayer at around 1060 cm^{-1}. This demonstrates that the effects of the free carrier concentration on the longest living bulk PPhP mode and LOPC mode are similar. In fact, the frequency of the plasmon electronic oscillation mode is directly proportional to the free carrier concentration and generally exceeds that of the zone center longitudinal optical phonon mode. Hence, when a plasmon electronic oscillation mode couples with a zone center longitudinal optical phonon mode (due to the macroscopic polarization field associated with both excitations), the resultant LOPC mode frequency broadens (i.e., its lifetime decreases) and shifts towards higher frequencies as the free carrier concentration increases. Thus, these observations clearly demonstrate the strong dependence of the longest living bulk PPhP mode on the free carrier concentration and LOPC mixed character mode frequency.

The mean-propagation-length of the bulk PPhP as a function of the free carrier concentration can be determined by considering in Eq. (13a) real frequency ω and a complex wavevector $k = k' + ik''$. The inverse of the function $k''(\omega)$ describes the frequency-dependent mean-propagation-length. The curves of the mean-propagation-length in Fig. 4 show analogous features to those of the lifetime curves. The peak mean-propagation-length value of the PPhP modes in the slightly implanted epilayer is almost 65% smaller than that of the PPhP modes in the un-implanted epilayer. It is worth noting that unlike the lifetime, the mean-propagation-length of the bulk PPhP in the crystal having the highest carrier concentration is slightly larger than that of the bulk PPhP in the two other crystals away from the resonance peak. This is

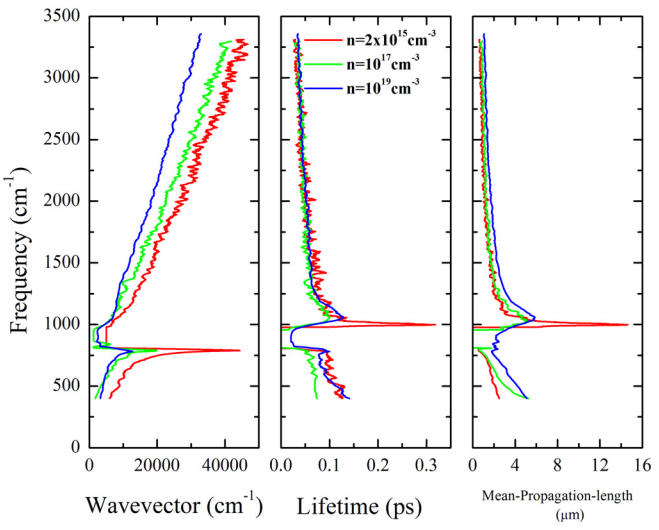

FIG. 4. Dispersion relations, lifetime, and mean-propagation length of the bulk plasmon-phonon-polariton in the samples investigated.

due to the speed at which the bulk PPhP propagates in the crystal. Comparing the slopes of the dispersion curves of the three crystals investigated, we notice that the PPhP modes in the crystal having the highest carrier concentration propagate the fastest, hence having a larger mean-propagation-length. The reason behind this is the fact that the real part of the refractive index decreases as the carrier concentration increases in the sample (see Fig. 2).

C. Surface plasmon-phonon-polariton

Let us now use the deduced complex dielectric functions of the three measured crystals to investigate the effect of the carrier concentration on the characteristics of the surface PPhP, which are surface modes created upon coupling between the incident electromagnetic field, the zone center optical phonon modes, and the free carriers' collective oscillation modes. After solving Maxwell's equations both inside and outside of an isotropic parallelepiped-like crystalline material and applying proper boundary conditions, one can write the dispersion relations of this surface wave in the form[41]

$$(ck)^2 = \frac{\varepsilon(\omega)}{1+\varepsilon(\omega)}\omega^2. \tag{14}$$

Likewise to bulk PPhP, solving Eq. (14) with considering complex ω leads to determining the surface mode lifetimes, and solving Eq. (14) with considering complex k leads to determining the mean-propagation-length of the surface modes. The dispersion curves, frequency-dependent lifetime, and frequency-dependent mean-propagation-length of the surface PPhP modes are plotted together in Fig. 5 for the three measured crystals. The surface modes are excited only in the frequency range where the real part of the complex dielectric function is negative. This range, which is known as the Reststrahlen band, is bounded by the zone center transverse and longitudinal optical mode frequencies. Furthermore, a typical dispersion curve of surface modes presents a frequency gap. This gap is revealed by a discontinuity in the dispersion curve if the damping rates of the LOPC modes are weak and by a negative slope if the damping rates of the LOPC modes are relatively high.

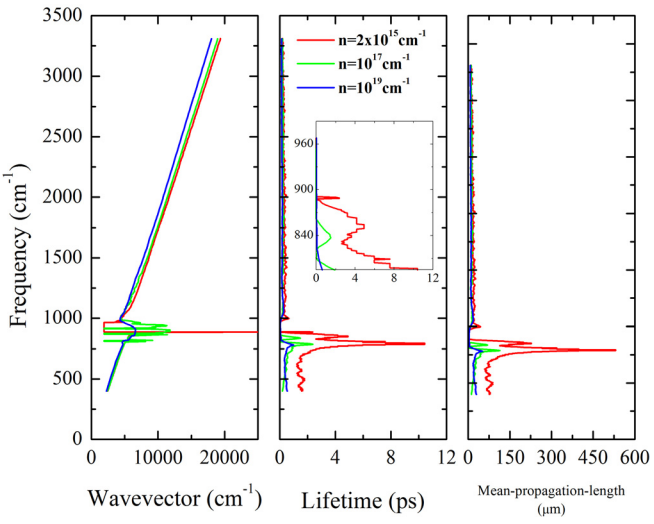

FIG. 5. Dispersion relations, lifetime, and mean-propagation length of the surface plasmon-phonon-polariton in the samples investigated. Inset: zoom in the region of existence of the surface plasmon-phonon-polariton.

It can be seen from Fig. 5 that the free carrier concentration also has a significant effect on the surface PPhP characteristics. However, the effect of the free carrier concentration on the surface PPhP is different from that on the bulk PPhP. The lifetime of the longest living surface PPhP mode decreases as the free carrier concentration is increased in the crystal, but the frequency of the longest living surface PPhP mode is independent of the free carrier concentration. Therefore, it appears that the frequency of the longest living surface PPhP depends of the frequency of the zone center transverse optical phonon modes whose frequencies are independent of the free carrier concentration in the volume.

In the lowest doped epilayer, the surface PPhP presents a peak lifetime value of 4.9 ps in its range of existence, which is much longer than the lifetime of pure surface plasmon modes, reaching up to 500 fs in their prime conditions, as reported by Woessner *et al.*[42] The surface PPhP lifetime is dropped by almost 98% as the free carrier concentration is increased, taking a value of 0.1 ps for the epilayer in which the carrier concentration is about $10^{19}\,\mathrm{cm}^{-3}$. Furthermore, examining the dispersion relation curves, we can notice that these waves propagate on the surface with a speed that is weakly affected by the free carrier concentration. For that reason, the plots of mean-propagation-length show the same dependence on the free carrier concentration as those of the lifetime. Accordingly, the surface PPhP waves propagating on the surface of the lowest doped sample show a peak mean-propagation-length value of 227.6 μm, which is dropped by almost 98% as the free carrier concentration is increased, taking the value of 4.8 μm.

D. Comparison between bulk and surface plasmon-phonon-polariton modes

Comparing the results obtained for bulk and surface PPhP, we see that the lifetimes and mean-propagation-lengths of the surface PPhP modes are much longer than those of the bulk PPhP modes. Moreover, the surface PPhP waves travel at a faster rate than the bulk PPhP waves. In Fig. 6, we plot the dispersion curves of both bulk and surface PPhP in the lowest doped sample to illustrate the difference in group velocities of these two waves. The bulk PPhP modes travel about 2.4 times slower than their surface counterparts, which is in agreement with the value of the real part of the refractive index obtained by the corrected Kramers-Kronig technique (see Fig. 2, $\mathrm{Re}(N) \sim 2.4$ away from resonance). However, the lifetimes of the surface PPhP modes are a stronger function of the carrier concentration. As mentioned earlier, the surface PPhP mode lifetime exhibits about 98% decay, while bulk PPhP exhibits only about 70% decay as the free carrier concentration is increased. This can be understood if we realize that, unlike volume plasmon modes, surface plasmon modes also possess transverse electric field components. This makes the PPhP coupling on the surface stronger than that in the volume and consequently enhances

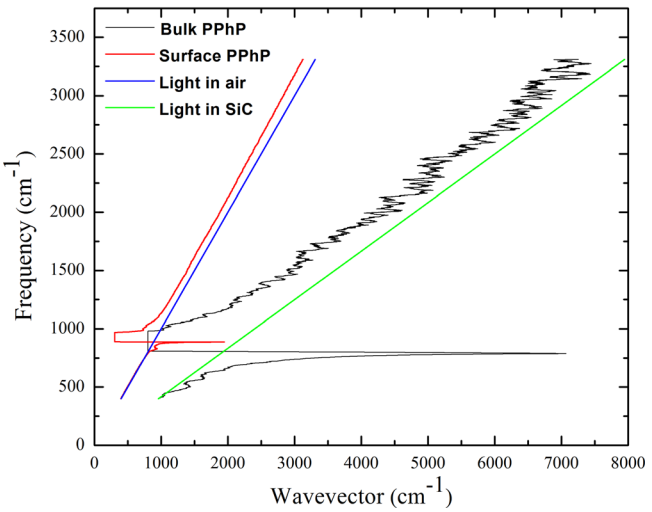

FIG. 6. Comparison between the surface plasmon-phonon-polariton (blue line) and bulk plasmon-phonon-polariton (red line) in the lowest doped 4 H-SiC epilayer. The light lines in air (black) and in 4 H-SiC (green) are also plotted.

the damping rate of the surface PPhP over that of the bulk PPhP.

E. Temporal coherence of the surface plasmon-phonon polariton modes

In the last couple of decades, surface phonon-polariton modes have captured remarkable interest because they showed unanticipated behavior.[4,14,15] It was demonstrated that the energy density of these waves is almost monochromatic. They also appear to have a long coherence time and a spatial coherence over distances much longer than their wavelengths. Therefore, it would be of particular interest to use the results presented above to draw a conclusion in respect of the effect of the free carrier concentration on the coherence of the surface plasmon-phonon-polariton waves. The width of the light spectrum is a measure of the temporal coherence of the emitting source. However, the width of the light spectrum is directly proportional to the width of the mode lifetime spectrum. Hence, the width of the surface PPhP lifetime peak that occurs in the Reststrahlen band (the region of existence of the surface phonon modes) is also a measure of temporal coherence of the surface PPhP. In the lowest doped crystal, the coherence time of the longest living mode takes the value of 0.75 ps (according to the Heisenberg uncertainty principle), but the increase in the free carrier concentration leads to unanticipated results. As shown in Fig. 5, as the carrier concentration is raised to $10^{17}\,cm^{-3}$, the coherence time is increased by 125% (narrower bandwidth) taking the value of 1.67 ps. Raising the free carrier concentration to $10^{19}\,cm^{-3}$, however, leads to an extremely high decay rate of surface PPhP modes, so that the surface PPhP modes barely survive in such a highly doped crystal and their coherence becomes undetectable. These results suggest the following: The surface plasmon modes, similarly to the surface phonon-polariton modes, have some degree of temporal coherence. Thus, although the coupling of the free carrier collective oscillation modes with the longitudinal optical phonon modes has a negative influence on the lifetime of the resultant surface PPhP modes, it can considerably enhance the temporal coherence of these resultant surface wave modes. Consequently, surface PPhP modes can be employed for the development of highly temporal coherent thermal sources, either completely new or through doping of existing ones.

V. CONCLUSION

In summary, we have investigated the dependence of the dispersion relations, lifetime, mean-propagation-length, and temporal coherence of the surface plasmon-phonon-polariton modes on the free carrier concentration in 4 H-SiC. The Fourier transform of *p*-polarized reflectivity spectra averaged over a wide incidence angle range were collected from 4 H-SiC epilayers of different carrier concentrations and used to precisely deduce the complex dielectric properties of the measured samples. The analysis of the measured reflectivity spectra consists in first deducing the complex dielectric functions of the measured samples using the Kramers-Kronig conversion method and then correcting the effects of the substrate response and artificial extrapolation of the measured reflectivity to zero and infinity using a numerical technique involving Fresnel equations for reflectivity from a multilayer system. We have found that, when the free carrier concentration is low in the sample, the lifetimes of the surface plasmon-phonon-polariton modes exceed by an order of magnitude the lifetimes of pure surface plasmon modes. However, they decrease rapidly as the free carrier concentration is increased in the sample. We have also shown that the coupling between the free carriers' collective oscillation, the zone center longitudinal optical phonon, and an incident electromagnetic wave leads to a highly temporal coherent surface plasmon-phonon-polariton wave. It is found that the temporal coherence of that resultant surface wave can be further enhanced by increasing the free carrier concentration in the sample. We believe that the outcomes of this work may open horizons in the field of nanophotonics where plasmon-phonon-polariton modes will be used as the main actors for controlling and manipulating light in the nanoscale regime.

ACKNOWLEDGMENTS

We would like to acknowledge the financial support by the National Council for Scientific Research (CNRS-Lebanon) and the American University of Beirut through a URB grant.

[1]S. Slussarenko, A. Alberucci, C. P. Jisha, B. Piccirillo, E. Santamato, G. Assanto, and L. Marrucci, Nat. Photonics **10**, 571 (2016).
[2]J. M. Merlo, N. T. Nesbitt, Y. M. Calm, A. H. Rose, L. D'Imperio, C. B. Yang, J. R. Naughton, M. J. Burns, K. Kempa, and M. J. Naughton, Sci. Rep. **6**, 31710 (2016).
[3]J. R. Fan, Z. Y. Li, Z. J. Chen, and W. G. Wu, Appl. Surf. Sci. **384**, 534 (2016).
[4]J. D. Caldwell, A. V. Kretinin, Y. Chen, V. Giannini, M. M. Fogler, Y. Francescato, C. T. Ellis, J. G. Tischler, C. R. Woods, A. J. Giles, M. Hong, K. Watanabe, T. Taniguchi, S. A. Maier, and K. S. Novoselov, Nat. Commun. **5**, 5221 (2014).
[5]J. D. Caldwell, I. Vurgaftman, J. G. Tischler, O. J. Glembocki, J. C. Owrutsky, and T. L. Reinecke, Nat. Nanotechnol. **11**, 9 (2016).
[6]A. de Hoogh, A. Opheij, M. Wulf, N. Rotenberg, and L. Kuipers, ACS Photonics **3**, 1446 (2016).

[7]F. Chiadini, V. Fiumara, A. Scaglione, and A. Lakhtakia, J. Opt. Soc. Am. B-Opt. Phys. **33**, 1197 (2016).
[8]J. Dong, J. G. Wang, F. C. Ma, Y. Cheng, H. Zhang, and Z. L. Zhang, Plasmonics **10**, 1841 (2015).
[9]J. D. Caldwell, L. Lindsay, V. Giannini, I. Vurgaftman, T. L. Reinecke, S. A. Maier, and O. J. Glembocki, Nanophotonics **4**, 44 (2015).
[10]J. B. Khurgin and A. Boltasseva, MRS Bull. **37**, 768 (2012).
[11]A. Boltasseva and H. A. Atwater, Science **331**, 290 (2011).
[12]C. F. Bohren and D. R. Hiffman, *Absorption and Scattering of Light by Small Particles* (Wiley-VCH, Weinheim, Germany, 1998), p. 241.
[13]S. Kojima and T. Mori, AIP Conf. Ser. **1627**, 52 (2014).
[14]J. D. Caldwell, O. J. Glembocki, Y. Francescato, N. Sharac, V. Giannini, F. J. Bezares, J. P. Long, J. C. Owrutsky, I. Vurgaftman, J. G. Tischler, V. D. Wheeler, N. D. Bassim, L. M. Shirey, R. Kasica, and S. A. Maier, Nano Lett. **13**, 3690 (2013).
[15]Y. G. Chen, Y. Francescato, J. D. Caldwell, V. Giannini, T. W. W. Mass, O. J. Glembocki, F. J. Bezares, T. Taubner, R. Kasica, M. H. Hong, and S. A. Maier, ACS Photonics **1**, 718 (2014).
[16]J.-J. Greffet, R. Carminati, K. Joulain, J.-P. Mulet, S. Mainguy, and Y. Chen, Nature **416**, 61 (2002).
[17]F. Marquier, K. Joulain, J.-P. Mulet, R. Carminati, and J.-J. Greffet, Phys. Rev. B **69**, 155412 (2004).
[18]R. Carminati and J.-J. Greffet, Phys. Rev. Lett. **82**, 1660 (1999).
[19]A. V. Shchegrov, K. Joulain, R. Carminati, and J.-J. Greffet, Phys. Rev. Lett. **85**, 1548 (2000).
[20]C. Henkel, K. Joulain, R. Carminati, and J.-J. Greffet, Opt. Commun. **186**, 57 (2000).
[21]J. A. Schuller, T. Taubner, and M. L. Brongersma, Nat. Photonics. **3**, 658 (2009).
[22]H. Harima, S. Nakashima, and T. Uemura, J. Appl. Phys. **78**, 1996 (1995).
[23]J. D. Caldwell, O. J. Glembocki, S. M. Prokes, E. R. Glaser, K. D. Hobart, D. M. Hansen, G. Chung, A. V. Bolotnikov, and T. S. Sudarshan, J. Appl. Phys. **101**, 093506 (2007).
[24]M. Schubert, T. Hofmann, and J. Sik, Phys. Rev. B **71**, 035324 (2005).
[25]Y. Ishitani, J. Appl. Phys. **112**, 063531 (2012).
[26]D. G. Piliposyan, K. B. Ghazaryan, and G. T. Piliposian, J. Phys. D **48**, 175501 (2015).
[27]L. Ottaviani, M. Kazan, S. Biondo, F. Tuomisto, F. Milesi, J. Duchaine, F. Torregrosa, and O. Palais, Mater. Sci. Forum **725**, 41 (2012).
[28]N. Rahbany, M. Kazan, M. Tabbal, R. Tauk, J. Jabbour, J. Brault, B. Damiliano, and J. Massies, J. Appl. Phys. **114**, 053505 (2013).
[29]G. Chen, in *Nanoscale Energy Transport and Conversion* (Oxford University Press, Inc., New York, 2005), pp. 174–188.
[30]M. Kazan, J. Appl. Phys. **102**, 073532 (2007).
[31]S. Ushioda and J. D. McMullen, Solid State Commun. **11**, 299 (1972).
[32]M. Kazan, S. Pereira, M. R. Correia, and P. Masri, J. Appl. Phys. **106**, 023523 (2009).
[33]M. Kazan, Ch. Zgheib, E. Moussaed, and P. Masri, Diamond Relat. Mater. **15**, 1169 (2006).
[34]V. I. Zemski, E. L. Ivchenko, D. N. Mirlin, and I. I. Reshina, Solid State Commun. **16**, 221 (1975).
[35]H. Yugami, S. Nakashima, A. Mitsuishi, A. Uemoto, M. Shigeta, K. Furukawa, A. Suzuki, and S. Nakajima, J. Appl. Phys. **61**, 354 (1987).
[36]T. Nakamura and T. Katoda, J. Appl. Phys. **55**, 3064 (1984).
[37]M. V. Klein, B. N. Ganguly, and P. J. Colwell, Phys. Rev. B **6**, 2380 (1972).
[38]G. Irmer, V. V. Toporov, B. H. Bairamov, and J. Monecke, Phys. Status Solidi B **119**, 595 (1983).
[39]M. Kazan, B. Rufflé, Ch. Zgheib, and P. Masri, Diamond Relat. Mater. **15**, 1525 (2006).
[40]R. W. Gammon and E. D. Palik, J. Opt. Soc. Am. **64**, 350 (1974).
[41]N. Marshall and B. Fischer, Phys. Rev. Lett. **28**, 811 (1972).
[42]A. Woessner, M. B. Lundeberg, Y. Gao, A. Principi, P. Alonso-González, M. Carrega, K. Watanabe, T. Taniguchi, G. Vignale, M. Polini, J. Hone, R. Hillenbrand, and F. H. L. Koppens, Nat. Mater. **14**, 421 (2015).